ACSNANO

www.acsnano.org

ARTICLE

Simultaneous Successive Twinning Captured by Atomic Electron Tomography

Philipp M. Pelz,[¶] Catherine Groschner,[¶] Alexandra Bruefach, Adam Satariano, Colin Ophus, and Mary C. Scott*

Cite This: *ACS Nano* 2022, 16, 588–596

Read Online

ACCESS | Metrics & More | Article Recommendations | Supporting Information

ABSTRACT: **Shape-controlled synthesis of multiply twinned nanostructures is heavily emphasized in nanoscience, in large part due to the desire to control the size, shape, and terminating facets of metal nanoparticles for applications in catalysis. Direct control of the size and shape of solution-grown nanoparticles relies on an understanding of how synthetic parameters alter nanoparticle structures during synthesis. However, while outcome populations can be effectively studied with standard electron microscopy methods, transient structures that appear during some synthetic routes are difficult to study using conventional high resolution imaging methods due to the high complexity of the 3D nanostructures. Here, we have studied the prevalence of transient structures during growth of multiply twinned particles and employed atomic electron tomography to reveal the atomic-scale three-dimensional structure of a Pd nanoparticle undergoing a shape transition. By identifying over 20 000 atoms within the structure and classifying them according to their local crystallographic environment, we observe a multiply twinned structure consistent with a simultaneous successive twinning from a decahedral to icosahedral structure.**

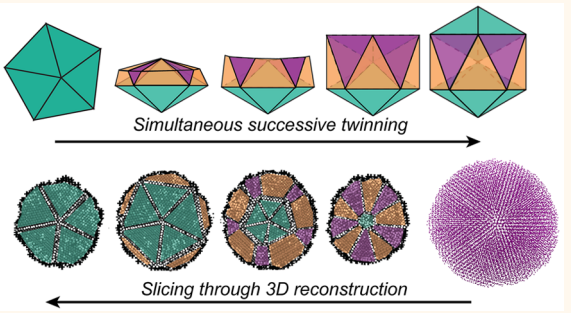

KEYWORDS: *electron microscopy, electron tomography, metal nanoparticles, successive twinning, multiply twinned nanoparticles, catalysis*

Multiply twinned particles (MTPs) are ubiquitous in solution-grown nanoparticle populations of face-centered cubic (fcc) metals. The ability to improve catalytic activity by controlling the exposed surface facet and strain states of the MTPs is a major driving force to understand their evolution during synthesis.[1−7] The primary MTPs that appear in fcc metal nanoparticle populations are decahedra and icosahedra, which have an idealized structure described by assemblies of 5 or 20 tetrahedral subunits respectively, with subunits joined by twin boundaries of close-packed ⟨111⟩-terminated surface facets. However, other multiply twinned structures are commonly observed, either as transient structures during synthesis[8,9] or as final reaction products.[10,11]

Studies of MTP synthesis have identified many possible growth pathways to generate MTPs.[3,8,9,12,13] Many efforts to create size and shape controlled MTPs center around controlling the population of nanometer-sized crystal seeds, which can uniformly grow into larger particles with the same shape *via* layer-by-layer growth.[14] However, other structural evolution pathways are known to occur during colloidal growth of MTPs, such as successive twinning and oriented attachment.[9,15] The successive twinning growth process is unique to MTPs and refers to the additive growth of new tetrahedra to multiply twinned structures. This process can evolve single tetrahedra into a more complex MTP by island-to-tetrahedron growth on one of the facets of the single tetrahedra.

The details of the successive twinning process are not clear. The decahedron to icosahedron successive twinning growth pathway is particularly difficult to quantitatively characterize using two-dimensional imaging methods given the complex overlapping crystal grain structure of these MTPs. Some studies have indicated that icosahedra can evolve from fully formed decahedra,[8,12] while others claim icosahedra generated through successive twinning require a partially formed decahedron.[16] These processes also differ in whether there is simultaneous extension of multiple grains or whether subsequent twinning does not happen until complete tetrahedron growth.[13] Furthermore, the role that local defects and surface structures play during successive twinning have not been identified.

Received: September 5, 2021
Accepted: November 5, 2021
Published: November 16, 2021

https://doi.org/10.1021/acsnano.1c07772
ACS Nano 2022, 16, 588–596

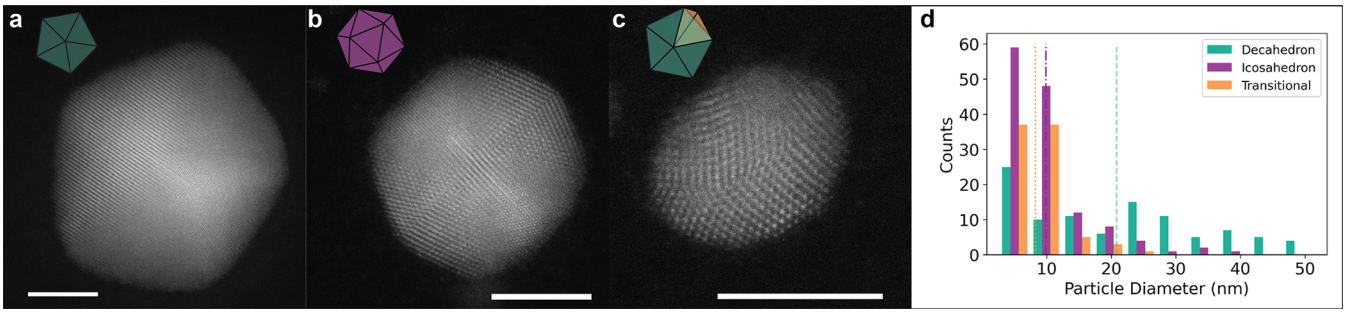

Figure 1. Representative images of the structures observed and histogram from the aliquot study. (a) Sample decahedron. (b) Sample icosahedron. (c) Sample particle transitioning between decahedron and icosahedron. (d) Histogram of the populations observed for the different structures as a function of size. Scale bar represents 5 nm.

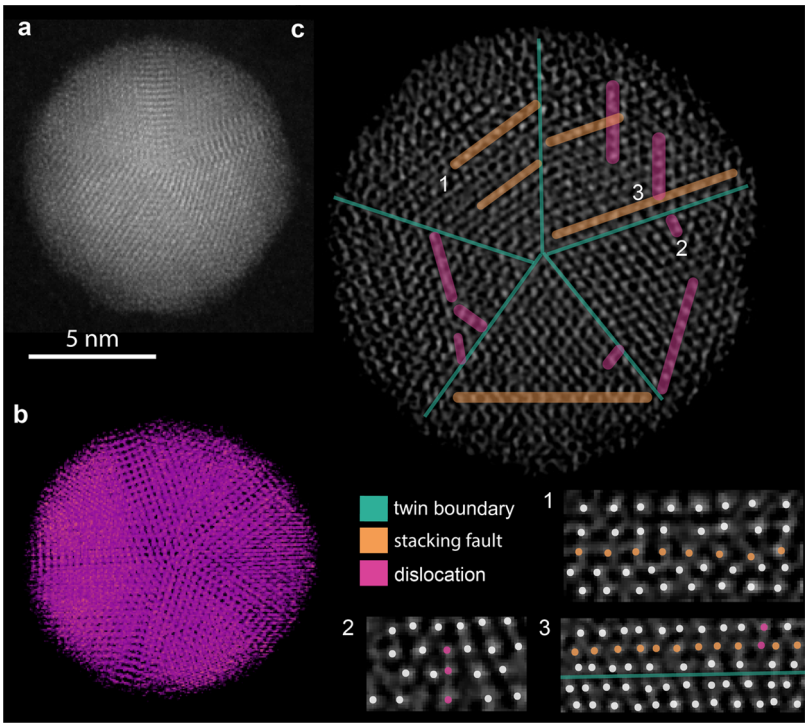

Figure 2. (a) Sample STEM micrograph from the tilt series. (b) Volumetric rendering of the tomographic reconstruction. (c) Example slice through the atomic volume normal to the 5-fold axis with various defects highlighted.

Electron microscopy characterization has been critical in our understanding of MTP particle stability and growth. Several examples of successive twinning have been observed using electron microscopy in both static and liquid cell experiments.[8,9,12] However, most previous experimental electron microscopy studies have been limited to two-dimensional imaging, such that many of the multitetrahedron stuctures present during successive twinning appear ambiguous. Atomic electron tomography (AET) is a method that utilizes high-resolution scanning transmission electron microscopy (HR-STEM) data sets to reconstruct the atomic-scale 3D structure of materials. Previous AET studies have resolved the structure, local defects, and strain in icosahedral and decahedral metal nanoparticles,[17,18] making it an ideal tool to resolve the complicated crystal structure of nanoparticles undergoing successive twinning.

In this work, we applied conventional HR-STEM to a population of Pd nanoparticles to determine the frequency of appearance of decahedra, icosahedra, and multiply twinned particles undergoing successive twinning, which we will refer to as multitetrahedron particles. AET was then used to measure the atomic-scale structure of a representative particle undergoing successive twinning. AET revealed significant structural disorder within the particle. The more than 20 000 atomic coordinates in 3D provided by AET analysis were further classified according to their local fcc or hexagonally close-packed (hcp) environment. This classification enabled atomic-scale 3D visualization of a simultaneous successive twinning process, where the particle was midway through a transformation from decahedron to icosahedron. We also observe stacking faults and other defects within the crystal grains of the particle, and a region of crystalline disorder on the surface of the particle.

RESULTS AND DISCUSSION

Population Statistics of Pd Nanoparticles. To understand the relationship between MTP size and structure, we first analyzed Pd nanoparticle populations using HR-STEM. Following previous work,[14] we used an aqueous synthesis

https://doi.org/10.1021/acsnano.1c07772
ACS Nano 2022, 16, 588−596

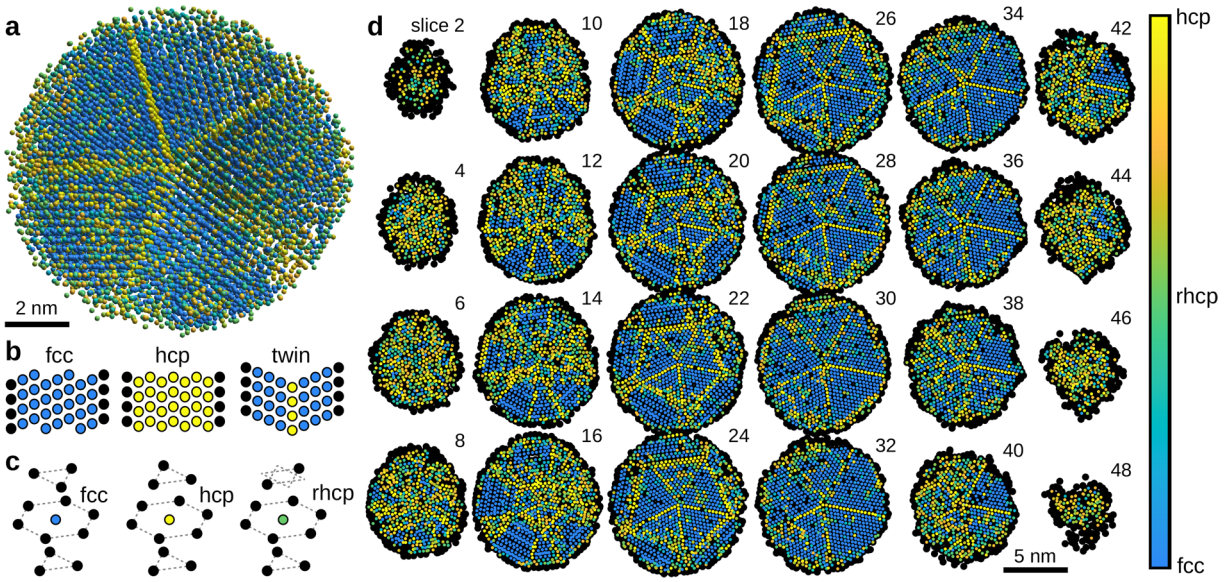

Figure 3. Crystallographic ordering of the atoms in the Pd MTP. (a) Traced atom positions with coordination numbers of 12, colored by fcc to hcp ordering. (b) Atomic stacking arrangement of fcc, hcp, and twinned structure view from the side. (c) 3D atomic neighborhood of sides with fcc, hcp, and rhcp ordering. (d) Slices throughout the MTP showing the crystallographic ordering for each atom with at least 10 neighboring sites.

known to produce decahedral particles that employs poly(vinyl pyrrolidone) (PVP) as a stabilizing agent and citrate as a reducing agent and capping agent. To broadly capture size and shape statistics, incubation time was varied from 1 to 24 h (Methods). Population statistics of the synthesized nanoparticles were manually determined from 691 particles identified in the HR-STEM data. Figure 1 summarizes the results of the HR-STEM study. The results confirm the presence of decahedra, iscoahedra, and multitetrahedron particles that appear to be undergoing a successive twinning process. Figure 1a–c shows sample micrographs of these structures. The size and shape distributions presented in Figure 1d show a clear size trend among the three structures. The icosahedra and successive twinning structures have size distributions skewed toward smaller sizes, with average sizes of 9.87 ± 0.57 nm and 8.28 ± 0.41 nm, respectively. The decahedra show a more uniform distribution with an average size of 20.8 ± 1.39 nm. The synthesis conditions used for this study were a relatively high concentration of reducing agent as well as a stabilizing agent (PVP) and should result primarily in decahedra.[14,19] Unlike other syntheses that use halogens to modify the reaction environment, the synthesis performed in this study does not employ such precursors.[20,21] While our method does not include these precursors, we still observe that an overwhelming majority of particles larger than 20 nm are decahedra. Since PVP primarily interacts with nanoparticles larger than 10 nm,[22] the PVP interaction with growing particles may be critical to stabilizing growing decahedra. This may explain why multitetrahedron and icosahedron particles are primarily observed at sizes below approximately 10 nm. Despite these observations, the limitations of studying three-dimensional structures through 2D micrographs limits the insights that can be made.

Atomic Electron Tomography of a Pd MTP. To obtain a detailed understanding of the three-dimensional atomic structure of an MTP undergoing successive twinning, we performed AET on a representative Pd particle. We used aberration-corrected STEM to collect a tilt series of 49 images of an approximately 10 nm diameter particle, with tilt angles ranging from −61 to 64° (Supporting Information Figure 1). Images taken before and after the tilt series acquisition indicate that the particle's structure did not change during imaging (Supporting Information Figure 2). While the particle's shape and crystal structure were largely consistent with a decahedron (Figure 2a), several images in the tilt series indicate the presence of additional crystalline grains in the nanoparticle, suggesting that the particle is undergoing successive twinning (Supporting Information Figure 1). After denoising and aligning the tilt series (Methods), we reconstructed the volume shown in Figure 2b using an advanced iterative reconstruction algorithm (Methods). To assess the consistency between the final reconstructed volume and the input projections, we define the *R*-factor as the pixel-wise difference of the absolute values of the measured and calculated projections from the reconstructed volume, normalized by the intensities of the measured projections. The *R*-factor of the final reconstruction was 8.1%, which is consistent with other reported AET reconstructions.[23]

After the final reconstruction volume was obtained, atomic positions were determined using an iterative 3D Gaussian fitting procedure. Atomic locations were included or excluded based on unsupervised clustering of the atoms based on atom intensities and radial distribution function of the atoms (Methods). Subsequently we determined the atom set that maximizes the Fourier Ring Information[24] between a linear image generated from the atom positions and the measured projections (see Methods for a detailed description). Using this method, we determined the atom positions of 20 632 atoms, shown in Figure 3a.

A qualitative analysis of the structures present in the reconstructed volume, shown in Figure 2b, reveals a large number of defects in the structure. To illustrate the large number of both stacking faults and dislocations in the particle, a 0.25 Å thick slice through the volume with defects highlighted is presented in Figure 2. Many of the stacking faults and associated dislocations are observed adjacent to the

https://doi.org/10.1021/acsnano.1c07772
ACS Nano 2022, 16, 588–596

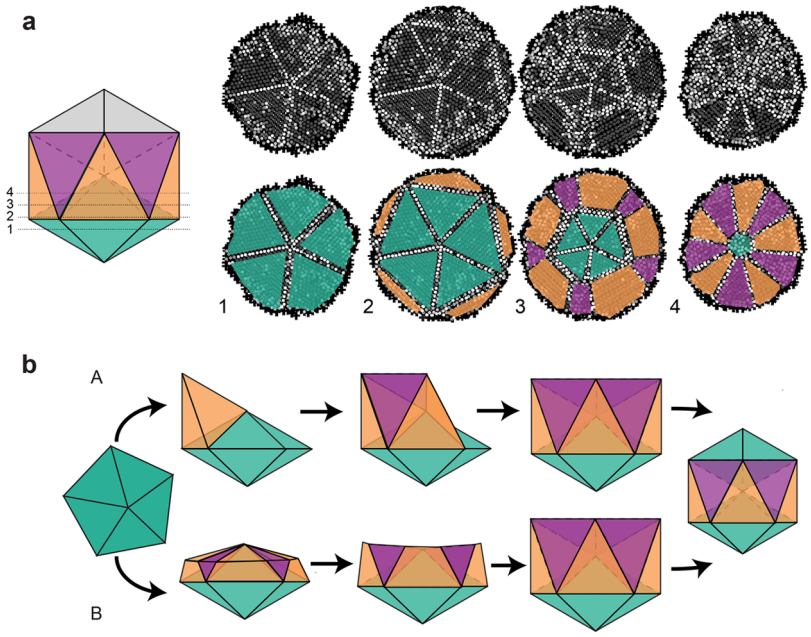

Figure 4. (a) Sample slices from the labeled atomic coordinates shown in Figure 3 labeled with how they would correspond to slices through an icosahedron. (b) Schematic of the two pathways observed for the successive twinning process.

twin boundaries, which was also observed in with molecular dynamics simulations of 5-fold twinned metal nanowires.[25] However, defects and disorder are not restricted to regions around the twin boundaries and can be found within the tetrahedral subunit bulk, as shown in defect 3 in Figure 2c). The number of stacking faults and edge dislocations observed in the reconstructed particle is much higher than in previous studies,[18,26] and we also see many more defects than predicted for nanomaterials of this size.[25] The stacking fault and twinning energy of fcc metals is in general low,[27] implying facile formation of stacking faults and twins during nanoparticle growth. Therefore, a possible explanation for the high number of defects in the particle is that the stacking fault mobility is slow compared to the rate of adatom addition to the particle. The synthesis procedure followed uses citric acid, a mild reducing agent, and takes several hours, which suggests slower, more thermodynamic growth conditions. Previous work has classified these synthesis methods as being broadly thermodynamically driven.[19] Though the overall synthesis has been hypothesized to be thermodynamically driven, twin boundary formation does increase the energy of the particle and may indicate local kinetic effects.[13] Given the overall slow growth, it is likely that the high number of defects comes from the highly strained structure of MTPs. Ideal fcc tetrahedra cannot be tiled into a decahedron or icosahedron in a way that is space filling.[28] MTP decahedra and icosahedra, consequently, must contain a high degree of internal strain because the crystal lattice must accommodate the missing volume.[29,30] Defects, such as stacking faults, are one mechanism for stress relief in MTPs.[30] Therefore, it is likely that the presence of the observed defects is also, at least in part, due to stress relief and is consistent with inhomogeneous strain within the particle.

Crystal Structure of Successively Twinning Particle. To better understand the crystal structure in the reconstructed particle, we classified the traced atom coordinates according to their crystallographic coordination. First, all sites were sorted according to their coordination number using a cutoff radius of 3.75 Å. Atoms with coordination numbers below 10 were classified as surface sites or highly disordered regions if they were fully contained in the nanoparticle. Most remaining sites in the particle bulk were primarily arranged into 4-atom tetrahedra. The most common structural packing of these tetrahedra was either fcc or hcp ordering. However, a large degree of disorder was present in many regions of the MTP on length scales larger than 4-atom clusters.

In order to determine the large scale structure of the MTP, we used a polyhedral matching algorithm inspired by Larsen *et al.*[31] to determine the degree of fcc and hcp ordering of each atomic shell. In this data set, we found that polyhedral matching produced much more robust identification of the differently ordered MTP regions than other methods such as local bond order parameters[32,33] or common neighbor analysis[34] (Supporting Information, Figure 6). A detailed description of the classification protocol is found in the Methods section. Briefly, for each valid atomic site, we defined polyhedra with vertices that correspond to fcc or hcp stacking geometries and fit them to the measured positions of the surrounding 12 atoms, depicted in Figure 3c. After rotating the polyhedra to minimize the distance between the ideal and measured atomic positions of the 12 nearest neighbors, we computed an order parameter for both fcc and hcp ordering (Methods). We then kept only the maximum order parameter for both fcc and hcp polyhedra. These values were used to determine the local ordering.

The results of this classification algorithm are shown in Figure 3. The 3D atomic coordinates with 12 nearest neighbors are shown in Figure 3a, where each site is colored according to the difference between the hcp and fcc order parameters defined above, from −1 to 1. The colors are strongly bimodal, indicating that the majority of sites possess either highly ordered hcp or fcc arrangements. The overall 5-fold symmetry of the nanoparticle is immediately obvious, though a significant amount of disorder is present both on the particle surface and in the bulk structure.

To visualize the structural ordering of the entire structure, we have plotted every other atomic slice of the particle in

https://doi.org/10.1021/acsnano.1c07772
ACS Nano 2022, 16, 588−596

Figure 3d, where the atoms are again colored by the difference between the hcp and fcc order parameters. Slices of the particle from five different viewing directions along the lattice of the tetrahedral subunits are available in Supporting Information Figure 7. Surface atoms are shown in black, as many of these sites do not have enough nearest neighbors to distinguish between fcc and hcp ordering. Figure 3b shows the two end point order parameters, the ideal fcc and hcp structures, viewed from the side. Figure 3b also shows a third structure motif that appears in many locations in Figure 3d, a twinned fcc structure, where a single line of atoms possessing high hcp ordering separates two fcc grains with mirrored structures. Figure 3c shows the 3D atomic arrangement of the two ideal polyhedra with fcc and hcp ordering, as well as a third structure that has the same order parameter for both structures (10 out of 12 possible sites agree with each class of polyhedron). This structure is labeled as random hexagonal closed packed (rhcp), following other studies that have used this label for packing falling between fcc and hcp.[35]

The obtained twinning structure reveals that the reconstructed particle contains a core decahedron, with additional, partially formed tetrahedra on top. The resultant structure is consistent with a partially formed icosahedron (Figure 4a). Considering the arrangement of partially formed tetrahedral subunits atop the decahedral core of the reconstructed nanoparticle, shown in Figure 4a, the particle seems to be captured in the midst of successively twinning and has partially transformed into an icosahedron. There are ten additional partially formed tetrahedra, forming two rows above the core decahedron. The tetrahedra closer to the decahedron are more fully formed. These nucleating tetrahedral units are highlighted in Figure 4a.

Prior observations of successive twinning have been in particles on the 100 nm scale and have shown tetrahedron by tetrahedron growth[8,10,12] illustrated schematically in Figure 4b, pathway A. However, the successive twinning we observe, illustrated in Figure 4b, pathway B, is better described as a simultaneous process, where the tetrahedra comprising the center portion of the icosahedra grow at the same time. This process more closely resembles the successive twinning process predicted for metal nanoclusters, where coordinated formation of a hcp layer across a decahedral surface leads to simultaneous twinning.[36,37] It is known that decahedra have more energetically stable hcp adatom sites than fcc,[36] making hcp island growth more probable, and therefore the growth of stacking faults and twin boundaries more probable, especially if there is limited surface diffusion. Our observations also directly confirm addition of multiple tetrahedra to a decahedral particle as a route toward an icosahedral structure.

CONCLUSION

In this study, we have determined the 3D atomic positions of over 20 000 atoms in a multiply twinned palladium nanoparticle. We have found that the structure derived from the aqueous synthesis contains substantially more defects than would be expected from previous computational and experimental studies. We directly observe a simultaneous successive twinning process wherein a decahedral particle is transitioning directly to an icosahedron. Based on our HR-STEM studies, we suspect this process would only occur in small decahedral nanoparticles under our reaction conditions, as after a certain size the structural directing PVP will have a stronger influence on growth.

The complex structure observed has implications for nanoparticle functionality. The lack of ⟨111⟩ terminating facets will significantly alter catalytic reactivity in a Pd particle. Similarly, the high number of defects in the particle's interior structure will change the surface strain states of the particle, which have will also affect catalytic activity.[1,38] Therefore, the combination of HR-STEM and AET used in this study provide insight into the structure and functionality of MTPs.

METHODS

Sample Preparation. All reagents used in this synthesis were purchased from Sigma-Aldrich. The Pd nanoparticle reaction was prepared based on the method reported by Lim *et al.*[14] with slight modifications. We used the conditions reported to synthesize a population of primarily decahedral particles. Briefly, a 15 mL three-necked flask was rinsed 3 times with Milli-Q water and acetone, then dried. The flask was equipped with a reflux condenser and Teflon-coated magnetic stir bar. A 4 mL aqueous solution containing poly(vinyl pyrrolidone) (PVP, 55 000 MW) and citric acid was transferred to the flask and heated to 90 °C while stirring using a heating mantle. Upon reaching 90 °C, a 1.5 mL solution of sodium tetrachloropalladate was rapidly added to the flask. For the aliquot study, samples were taken at 1, 3, 6, 8, 10, and 24 h. The final product was isolated by adding a 300 μL aliquot of acetone to 100 μL of nanoparticle solution in a clean microcentrifuge tube and centrifuged for 30 min at 13 000 rpm. The supernatant was decanted, and the pellet was resuspended in 300 μL of ethanol. The wash and rinse was repeated 2 times, and the purified particles were stored in Milli-Q water. The aqueous solution of Pd particles was deposited *via* nebulizer on a SiN window. The tomography study utilized a sample taken after incubating for 8 h.

Data Acquisition. Several tomographic tilt series were acquired from Pd nanoparticles using the TEAM 0.5 microscope and TEAM stage[39] at the National Center for Electron Microscopy in the Molecular Foundry. Images were acquired at 200 kV in ADF-STEM mode with a 25 mrad convergence semiangle (resulting in a probe size of 0.8 Å) and 41 and 210 mrad detector inner and outer semiangles. The tilt series was collected at 49 angles with a tilt range of 64° to −61°. Two images per tilt angle were measured with 3 μs dwell time with a scan rotation of 0° and 90° to minimize image blurring. The probe step was 17.3 pm, and STEM images were recorded with 1024 × 1024 pixels. The beam current was below the readable limit of 40 pA of the microscope flu-cam, which corresponds to a total fluence of less than 3.1×10^6 $e/Å^2$. The time required per tilt step was roughly 3 min, leading to a best-case total acquisition time of 2.45 h. Owing to imperfections in the calibration of the *x*- and *y*-scanning coils in the microscope's STEM scanning system, an additional correction was applied to the images to ensure square pixels. This scan distortion was measured using a standard sample under the same imaging conditions, and corrected using the method described by Ophus et al.[40]

Image Denoising. The drift-corrected images were denoised with the BM3D algorithm,[41] with Anscombe variance-stabilizing transform and its inverse applied before and after denoising.[42]

Tomographic Reconstruction. After denoising, the 49 images were projected onto the tilt axis and aligned with subpixel cross-correlation among the 1D-curves. A constant intensity scaling factor was fitted to the 1D curves to account for nonlinearities in the intensity at high tilt angles. Then the images were aligned to neighboring tilts with 2D subpixel cross-correlation. From the initially aligned tilt series a 3D reconstruction was performed using the fast adaptive shrinkage-thresholding algorithm (FASTA), an accelerated gradient algorithm with adaptive step size for faster convergence.[43] To compute the forward and backward projections, we used the generalized ray transform interface of the Operator Discretization Library[44] in a 3D parallel-beam Euler geometry with a GPU-accelerated backend of the ASTRA tomography toolbox.[45] To increase the accuracy of the projections, we used the trilinear interpolation feature of the ASTRA library to compute the forward and inverse ray-transforms. The code is freely available https://github.

https://doi.org/10.1021/acsnano.1c07772
ACS Nano 2022, 16, 588−596

com/PhilippPelz/fasta-tomography on Github. To minimize the translational and angular misalignments, we use a projection matching approach[46] with simulated annealing, where all three Euler angles are varied by a randomly picked value in the range of −0.5° to 0.5° and the calculated projection error is compared with the current projection error after a full reconstruction. The lowest-error angles are then used as new initial angles for the next tomographic reconstruction. This process is repeated for 10 outer iterations, and the random Euler angle perturbation reduced linearly every iteration. Using this approach, the reconstruction converged to an *R*-factor of 8.1%.

Atom Tracing and Classification. The 3D atomic positions of the Pd atoms were determined using the following procedure based on the code provided by Ren *et al.*[47] (I) All local intensity maxima were identified from the 3D reconstruction and added to a candidate list. From the initial candidate list, peaks that were within a minimum distance of 2.2 Å of a higher-intensity peak were deleted. (II) The initial list of peak positions was refined by fitting a 3D Gaussian function to each peak after subtracting neighboring peaks within a maximum radius of 4 Å. Using this initial atom candidate list, we added, refined, and merged new unidentified peaks for 4 iterations in the following order: (III) subtract the fitted Gaussians of all current peak candidates from the reconstruction volume; (IV) add new candidate peaks over an intensity threshold of 50 to the candidate list; (V) refine the positions of all atom candidates as in step II for 4 iterations; (VI) merge peaks that are closer than a minimum distance of 2.2 Å after position refinement; (VII) refine the positions of all atom candidates as in step II for 4 iterations; (VIII) go to step III if iterations not done. (IX) A final set of 4 position refinement iterations as in step II yielded the final set of 22 412 3D candidate atom positions, fitted atom intensities, and fitted Gaussian standard deviations.

The task of dividing the fitted atom candidates into real atoms and non-atoms can be seen as a binary classification problem if only one element is present or as a multiclass classification problem if more than one element is present. Previous work by Xu *et al.*[48] used the fitted Gaussian peak intensity as the determining feature to classify the atom candidates into atoms and non-atoms, and this procedure was later extended to two atomic species by Yang *et al.*,[42] and more than two atomic species by Yang, Zhou, Zhu, Yuan *et al.*[23] Starting from the lowest-intensity atom candidates, the method uses an atom flipping procedure to eliminate low-intensity atom candidates whose addition does not decrease the experimental error, and some manual decisions to clean up atomic coordinates in the end. Differences in the fitted peak intensity and size stem from experimental uncertainties, such as missing wedge artifacts, residual intensity from the substrate, nonlinearities due do multiple scattering, surface modifications during the experiment, or other intensity contributions, and are therefore expected to be more pronounced for large the missing wedges and thick samples. Promising developments to reduce these artifacts are focal series tomography[49,50] to extend the technique to thicker samples, sparsity-exploiting reconstruction methods that use minimal distance-constraints and atomicity directly in the tomographic reconstruction, supervised neural-network architectures for postfiltering tomographic reconstructions,[51] and differentiable probabilistic models[52] to replace the best-fit criteria for atom tracing with robust uncertainty estimates.

For our data set, we found that some low-intensity atom candidates were present in the center of the particle, making them unlikely candidates for the non-atom class and making the scalar fitted intensity alone an unreasonable choice as classification feature. Therefore, in addition to the fitted scalar intensity, we included other features of the reconstructed volume and the atom fitting procedure into the classification algorithm to eliminate non-atoms from the atom candidate list and prevent exclusion of atom candidates in the center of the particle.

For each atom candidate, we computed the radial distribution function (RDF) and split it up into 7 radial regions corresponding to sections between the peaks of the total RDF (see Supporting Information, Figure 4a). The sectioned RDF (8 floating-point values) together with the fitted peak intensity (scalar floating-point value), fitted peak standard deviation (scalar floating-point value), and reconstructed voxel intensities around the peak in a 2 Å radius (1408 floating-point values) then formed a 1429-dimensional feature vector for each atom candidate that we used to classify the peaks into atoms and non-atoms.

We first used the Uniform Manifold Approximation and Projection (UMAP)[53] method, a nonlinear dimensionality reduction technique, to project the high-dimensional feature vector onto a 2-dimensional manifold, which is shown in the Supporting Information (Figure 3g–j). On the left end of this manifold, we identified peaks at the surface of the particle with disordered nearest neighbors and low intensity, suggesting that this two-dimensional manifold is suitable for classification of the candidate peaks into atoms and non-atoms.

We then used a Bayesian Gaussian Mixture Model (BGMM)[54,55] to classify the candidate list using their UMAP-reduced two-dimensional features into two classes of potential atoms and non-atoms. A two-class BGMM models an *n*-dimensional point cloud as being generated from a sum of two Gaussian distributions and fits the covariance and location of the Gaussian distributions. For each atom candidate, the BGMM produces a probability of the candidate belonging to one of the two classes, in our case the atom and non-atom classes. Instead of the fitted scalar peak intensity, as in Yang *et al.*,[42] we used the probability of belonging to the Gaussian centered on the left side of the 2D manifold, around the atoms at the surface of the particle, as the discerning scalar feature in our atom flipping procedure. We first ranked the candidates according to their probability to belong to the non-atom class. To select the best probability threshold for including atoms in the non-atom class, we performed ADF-STEM simulations (see the following section) to generate multiple simulated tilt series for different BGMM probability thresholds. The simulated tilt series images were then compared with the experimental tilt series images using the Fourier Ring Information (FRI) criterion[24] to find the BGMM probability threshold that extracts the largest amount of information from the experimental data. The results are displayed in Supporting Information, Figure 3b, where the FRI displays a peak at 99.994%, and then drops off when more atoms candidates are included. We found that a threshold of 99.994% extracted the maximum amount of FRI from the data. We then finalized the set of atoms by performing the following atom-flipping procedure to determine if an atom within the bracket from 99.99% to 99.997% should be added. For each atom that falls in this probability range, we simulated a tilt series with and without that atom and compared the resulting FRI, using a simple linear image formation model, with the image being a linear sum of 3D Gaussian distributions for each atom, and the standard deviation determined from the atom fitting procedure. If addition of an atom increases the FRI, we included it in the list of atoms, otherwise we excluded it. This procedure yielded a final set of 20 632 Pd atoms in the particle.

STEM Simulations and Tracing Precision. For atom classification and to evaluate the self-consistency of the atom tracing procedure, we recreated the tilt series of 49 projections with the refined experimental Euler angles from the traced coordinates with quantum mechanical STEM simulations using the PRISM algorithm[56] implemented in the Prismatic simulation software.[57] A total of 49 cubic super cells of size $(11\ \text{nm})^3$ was created. The final atomic model was placed within the super cells. Individual super cells were divided into 2 Å slices along the beam direction and sampled with a pixel size of 12 pm in the transverse direction. The experimental parameters of 200 kV high tension, 25 mrad convergence semiangle, 41 and 210 mrad detector inner and outer semiangles, and 0 mm C_3 aberration were used for the simulation, and the focus of the probe was placed in the center of the simulation cell. We employed a Fourier interpolation factor of 5 in the PRISM algorithm and simulated 8 frozen phonon configurations. We matched the probe step to the reconstruction voxel size of 25 pm. Each simulated ADF-STEM image was convolved with a Gaussian function to simulate incoherent source spread and other incoherent effects and minimize the difference to experimental images. A 3D volume was then reconstructed from the simulated tilt series with the FASTA algorithm described above, and a new model

https://doi.org/10.1021/acsnano.1c07772
ACS Nano 2022, 16, 588–596

was obtained by using the same atom tracing procedure. The new atomic coordinates were rotated and translated using the iterative closest point algorithm[58] to minimize the global position deviations between the models. Then atoms were matched between the models and a root-mean-square displacement calculated between the models, with a radial search cutoff of 1.5 Å around each atom; 93% of the atoms could be matched between the experimentally traced coordinates and the retraced simulated coordinates. This corresponds to 19 160 paired sites out of 20 632 experimental sites. A histogram of the deviation between the common atom pairs is shown in Supporting Information, Figure 5a,b, indicating a RMS deviation of 37.4 pm for all sites and RMS deviation of 35 pm for bulk sites with 12 nearest neighbors. This is slightly higher than the RMS deviation of previous AET studies,[42] which we attribute to the relatively low number of projection measurements available relative to the size of the reconstructed particle. As shown in Supporting Information Figure 5e,f in a side-by-side comparison of the order parameters of the experimentally determined atoms and the retraced atoms from simulation, this RMS deviation is not large enough to change the appearance of the grains identified in this particle and confirms our observation of simultaneous successive twinning in this particle.

Atom Classification. To classify traced atoms according to their crystallographic coordination, we first generated polyhedra with 12 vertices $\mathbf{p}_j$ arranged in both fcc and hcp stacking geometries with nearest neighbor spacing equal to the mean measured value of 2.93 Å. These polyhedra are rotated to 1026 orientations roughly evenly spaced on 1/12th of the unit sphere. For each atomic site, these polyhedra were rotated using a matrix $\mathbf{m}$ to minimize the total distance between their (ideal) coordinates and the nearest relative atomic site using the iterative closest point (ICP) algorithm.[59] Finally we compute an order parameter for each polyhedra at each site s_k equal to

$$s_k = \sum_{j=1}^{12} \max\left(1 - \frac{|\mathbf{r}_j - \mathbf{r}_k - \mathbf{m}\mathbf{p}_j|}{d_{\max}}, 0\right) \quad (1)$$

where $\mathbf{r}_j$ is the position of the jth neighboring coordinate to site k at position $\mathbf{r}_k$, and $d_{\max}$ is maximum allowed distance of a site from an ideal position, which we set equal to half the average nearest neighbor distance of 1.47 Å. This cost function can generate values of 0 to 12, where a value of 12 indicates perfect alignment between the polyhedral template. We kept only the maximum order parameter (best agreement) for both fcc and hcp polyhedra and used these values to determine the local ordering.

We have also implemented bond-order parameter analysis by spherical harmonics.[60] A comparison of the different crystalline order parameter calculation methods is shown in Supporting Information Figure 6. Overall, we found the polyhedral matching analysis more robust to experimental noise.

ASSOCIATED CONTENT

Supporting Information

The Supporting Information is available free of charge at https://pubs.acs.org/doi/10.1021/acsnano.1c07772.

Full tomographic tilt series, before and after tomography micrographs of particle, explanatory scatter plots for atom classification by UMAP and BGMM, radial distribution function before and after atom classification, RMS deviations and order parameters precision for atom tracing, order parameter method comparison, and side views of the MTP (PDF)

AUTHOR INFORMATION

Corresponding Author

Mary C. Scott − *Department of Materials Science and Engineering, University of California Berkeley, Berkeley, California 94720, United States; The National Center for Electron Microscopy, Molecular Foundry, Berkeley, California 94720, United States*; Email: mary.scott@berkeley.edu

Authors

Philipp M. Pelz − *Department of Materials Science and Engineering, University of California Berkeley, Berkeley, California 94720, United States; The National Center for Electron Microscopy, Molecular Foundry, Berkeley, California 94720, United States*

Catherine Groschner − *Department of Materials Science and Engineering, University of California Berkeley, Berkeley, California 94720, United States*; orcid.org/0000-0001-9397-176X

Alexandra Bruefach − *Department of Materials Science and Engineering, University of California Berkeley, Berkeley, California 94720, United States*

Adam Satariano − *Department of Materials Science and Engineering, University of California Berkeley, Berkeley, California 94720, United States*

Colin Ophus − *The National Center for Electron Microscopy, Molecular Foundry, Berkeley, California 94720, United States*; orcid.org/0000-0003-2348-8558

Complete contact information is available at: https://pubs.acs.org/10.1021/acsnano.1c07772

Author Contributions

¶P.M.P. and C.G. contributed equally to this work. M.C.S. conceived the overall project. A.B. and A.S. synthesized the nanoparticles. C.G. collected particle size data and tilt series. P.M.P. reconstructed the particle. P.M.P. and C.O. performed the atom tracing. P.M.P. performed STEM simulations. P.M.P. and C.O. performed precision calculations. C.O. implemented ordering classification. C.G. and M.C.S. wrote the manuscript. All authors commented on the manuscript.

Notes

The authors declare no competing financial interest.

ACKNOWLEDGMENTS

We are grateful to P. Ercius for help with the calibration of the collection angles of the ADF detector. Work at the Molecular Foundry was supported by the Office of Science, Office of Basic Energy Sciences, of the U.S. Department of Energy under Contract No. DE-AC02-05CH11231. C.O. is supported by the USA Department of Energy Early Career Research Award program. P.M.P and M.C.S are supported by the Strobe STC research center, Grant No. DMR 1548924. This research was partially supported by the National Science Foundation under award number 1848079. C.K.G. is supported by the National Science Foundation Graduate Research Fellowship under Grant No. DGE-1752814.

REFERENCES

(1) Choi, S.-I.; Herron, J. A.; Scaranto, J.; Huang, H.; Wang, Y.; Xia, X.; Lv, T.; Park, J.; Peng, H.-C.; Mavrikakis, M.; Xia, Y. A Comprehensive Study of Formic Acid Oxidation on Palladium Nanocrystals with Different Types of Facets and Twin Defects. *ChemCatChem* **2015**, *7*, 2077−2084.

(2) Li, Y.; Cui, F.; Ross, M. B.; Kim, D.; Sun, Y.; Yang, P. Structure-Sensitive CO2 Electroreduction to Hydrocarbons on Ultrathin 5-Fold Twinned Copper Nanowires. *Nano Lett.* **2017**, *17*, 1312−1317.

(3) Xia, Y.; Xiong, Y.; Lim, B.; Skrabalak, S. E. Shape-Controlled Synthesis of Metal Nanocrystals: Simple Chemistry Meets Complex Physics? *Angew. Chem., Int. Ed.* **2009**, *48*, 60−103.

(4) Narayanan, S.; Cheng, G.; Zeng, Z.; Zhu, Y.; Zhu, T. Strain Hardening and Size Effect in Five-Fold Twinned Ag Nanowires. *Nano Lett.* **2015**, *15*, 4037−4044.
(5) Li, H.; Qiang, W.; Vuki, M.; Xu, D.; Chen, H.-Y. Fluorescence Enhancement of Silver Nanoparticle Hybrid Probes and Ultrasensitive Detection of IgE. *Anal. Chem.* **2011**, *83*, 8945−8952.
(6) Pietrobon, B.; Kitaev, V. Photochemical Synthesis of Monodisperse Size-Controlled Silver Decahedral Nanoparticles and Their Remarkable Optical Properties. *Chem. Mater.* **2008**, *20*, 5186−5190.
(7) Wang, X.; Vara, M.; Luo, M.; Huang, H.; Ruditskiy, A.; Park, J.; Bao, S.; Liu, J.; Howe, J.; Chi, M.; Xie, Z.; Xia, Y. Pd@ Pt Core−Shell Concave Decahedra: A Class of Catalysts for the Oxygen Reduction Reaction with Enhanced Activity and Durability. *J. Am. Chem. Soc.* **2015**, *137*, 15036−15042.
(8) Langille, M. R.; Zhang, J.; Mirkin, C. A. Plasmon-Mediated Synthesis of Heterometallic Nanorods and Icosahedra. *Angew. Chem., Int. Ed.* **2011**, *50*, 3543−3547.
(9) Ma, X.; Lin, F.; Chen, X.; Jin, C. Unveiling Growth Pathways of Multiply Twinned Gold Nanoparticles by in Situ Liquid Cell Transmission Electron Microscopy. *ACS Nano* **2020**, *14*, 9594−9604.
(10) Hofmeister, H. Habit and Internal Structure of Multiply Twinned Gold Particles on Silver Bromide Films. *Thin Solid Films* **1984**, *116*, 151−162.
(11) Hofmeister, H. Shape Variations and Anisotropic Growth of Multiply Twinned Nanoparticles. *Zeitschrift für Kristallographie* **2009**, *224*, 528−538.
(12) Langille, M. R.; Zhang, J.; Personick, M. L.; Li, S.; Mirkin, C. A. Stepwise Evolution of Spherical Seeds into 20-fold Twinned Icosahedra. *Science* **2012**, *337*, 954−957.
(13) Du, J. S.; Zhou, W.; Rupich, S. M.; Mirkin, C. A. Twin Pathways: Discerning the Origins of Multiply Twinned Colloidal Nanoparticles. *Angew. Chem., Int. Ed.* **2021**, *60*, 6858−6863.
(14) Lim, B.; Xiong, Y.; Xia, Y. A Water-Based Synthesis of Octahedral, Decahedral, and Icosahedral Pd Nanocrystals. *Angew. Chem., Int. Ed.* **2007**, *46*, 9279−9282.
(15) Song, M.; Zhou, G.; Lu, N.; Lee, J.; Nakouzi, E.; Wang, H.; Li, D. Oriented Attachment Induces Fivefold Twins by Forming and Decomposing High-Energy Grain Boundaries. *Science* **2020**, *367*, 40−45.
(16) Tsuji, M.; Ogino, M.; Matsuo, R.; Kumagae, H.; Hikino, S.; Kim, T.; Yoon, S.-H. Stepwise Growth of Decahedral and Icosahedral Silver Nanocrystals in DMF. *Cryst. Growth Des.* **2010**, *10*, 296−301.
(17) Scott, M. C.; Chen, C.-C.; Mecklenburg, M.; Zhu, C.; Xu, R.; Ercius, P.; Dahmen, U.; Regan, B. C.; Miao, J. Electron Tomography at 2.4-Angstrom Resolution. *Nature* **2012**, *483*, 444−447.
(18) Goris, B.; De Beenhouwer, J.; De Backer, A.; Zanaga, D.; Batenburg, K. J.; Sanchez-Iglesias, A.; Liz-Marzan, L. M.; Van Aert, S.; Bals, S.; Sijbers, J.; Van Tendeloo, G. Measuring Lattice Strain in Three Dimensions through Electron Microscopy. *Nano Lett.* **2015**, *15*, 6996−7001.
(19) Xiong, Y.; Xia, Y. Shape-Controlled Synthesis of Metal Nanostructures: The Case of Palladium. *Adv. Mater.* **2007**, *19*, 3385−3391.
(20) Xia, X.; Xie, S.; Liu, M.; Peng, H.-C.; Lu, N.; Wang, J.; Kim, M. J.; Xia, Y. On The Role of Surface Diffusion in Determining the Shape or Morphology of Noble-Metal Nanocrystals. *Proc. Natl. Acad. Sci. U. S. A.* **2013**, *110*, 6669−6673.
(21) Nalajala, N.; Chakraborty, A.; Bera, B.; Neergat, M. Chloride (Cl-) Ion-Mediated Shape Control of Palladium Nanoparticles. *Nanotechnology* **2016**, *27*, 065603.
(22) Koczkur, K. M.; Mourdikoudis, S.; Polavarapu, L.; Skrabalak, S. E. Polyvinylpyrrolidone (PVP) in Nanoparticle Synthesis. *Dalton Transactions* **2015**, *44*, 17883−17905.
(23) Yang, Y.; Zhou, J.; Zhu, F.; Yuan, Y.; Chang, D. J.; Kim, D. S.; Pham, M.; Rana, A.; Tian, X.; Yao, Y.; Osher, S. J.; Schmid, A. K.; Hu, L.; Ercius, P.; Miao, J. Determining the Three-Dimensional Atomic Structure of an Amorphous Solid. *Nature* **2021**, *592*, 60−64.
(24) van Heel, M.; Schatz, M. Information: To Harvest, to Have and to Hold. *arXiv (Image and Video Processing)*, 2020, http://arxiv.org/abs/2009.03223 (accessed November 1, 2021).
(25) Zhou, Y.; Fichthorn, K. A. Internal Stress-Induced Orthorhombic Phase in 5-Fold-Twinned Noble Metal Nanowires. *J. Phys. Chem. C* **2014**, *118*, 18746−18755.
(26) Hofmeister, H. Lattice Defects in Decahedral Multiply Twinned Particles of Palladium. *Z. Phys. D: At., Mol. Clusters* **1991**, *19*, 307−310.
(27) Rosengaard, N.; Skriver, H. L. Calculated Stacking-Fault Energies of Elemental Metals. *Phys. Rev. B: Condens. Matter Mater. Phys.* **1993**, *47*, 12865.
(28) Bagley, B. G. A Dense Packing of Hard Spheres with Five-Fold Symmetry. *Nature* **1965**, *208*, 674−675.
(29) Ino, S. Stability of Multiply-Twinned Particles. *J. Phys. Soc. Jpn.* **1969**, *27*, 941−953.
(30) Howie, A.; Marks, L. D. Elastic Strains and the Energy Balance for Multiply Twinned Particles. *Philos. Mag. A* **1984**, *49*, 95−109.
(31) Larsen, P. M.; Schmidt, S.; Schiøtz, J. Robust Structural Identification via Polyhedral Template Matching. *Modell. Simul. Mater. Sci. Eng.* **2016**, *24*, 055007.
(32) Steinhardt, P. J.; Nelson, D. R.; Ronchetti, M. Bond-Orientational Order in Liquids and Glasses. *Phys. Rev. B: Condens. Matter Mater. Phys.* **1983**, *28*, 784.
(33) Lechner, W.; Dellago, C. Accurate Determination of Crystal Structures Based on Averaged Local Bond Order Parameters. *J. Chem. Phys.* **2008**, *129*, 114707.
(34) Faken, D.; Jónsson, H. Systematic Analysis of Local Atomic Structure Combined with 3D Computer Graphics. *Comput. Mater. Sci.* **1994**, *2*, 279−286.
(35) Harke, B.; Ullal, C. K.; Keller, J.; Hell, S. W. Three-Dimensional Nanoscopy of Colloidal Crystals. *Nano Lett.* **2008**, *8*, 1309−1313.
(36) Baletto, F.; Ferrando, R. Island Adsorption and Adatom Diffusion on 3D Non-Crystalline Silver Nanoclusters. *Surf. Sci.* **2001**, *490*, 361−375.
(37) Baletto, F.; Ferrando, R. Structural Properties of Nanoclusters: Energetic, Thermodynamic, and Kinetic Effects. *Rev. Mod. Phys.* **2005**, *77*, 371−423.
(38) Huang, H.; Jia, H.; Liu, Z.; Gao, P.; Zhao, J.; Luo, Z.; Yang, J.; Zeng, J. Understanding of Strain Effects in the Electrochemical Reduction of CO2: Using Pd Nanostructures as an Ideal Platform. *Angew. Chem., Int. Ed.* **2017**, *56*, 3594−3598.
(39) Ercius, P.; Boese, M.; Duden, T.; Dahmen, U. Operation of TEAM I in a User Environment at NCEM. *Microsc. Microanal.* **2012**, *18*, 676−683.
(40) Ophus, C.; Ciston, J.; Nelson, C. T. Correcting Nonlinear Drift Distortion of Scanning Probe and Scanning Transmission Electron Microscopies from Image Pairs with Orthogonal Scan Directions. *Ultramicroscopy* **2016**, *162*, 1−9.
(41) Danielyan, A.; Katkovnik, V.; Egiazarian, K. BM3D Frames and Variational Image Deblurring. *IEEE Transactions on Image Processing* **2012**, *21*, 1715−1728.
(42) Yang, Y.; Chen, C.-C.; Scott, M. C.; Ophus, C.; Xu, R.; Pryor, A.; Wu, L.; Sun, F.; Theis, W.; Zhou, J.; Eisenbach, M.; Kent, P. R. C.; Sabirianov, R. F.; Zeng, H.; Ercius, P.; Miao, J. Deciphering Chemical Order/Disorder and Material Properties at the Single-Atom Level. *Nature* **2017**, *542*, 75−79.
(43) Goldstein, T.; Studer, C.; Baraniuk, R. A Field Guide to Forward-Backward Splitting with a FASTA Implementation. *arXiv (Numerical Analysis)*, 2014, http://arxiv.org/abs/1411.3406, (accessed November 1, 2021).
(44) Adler, J.; Kohr, H.; Ringh, A.; Moosmann, J.; sbanert; Ehrhardt, M. J.; Lee, G. R.; niinimaki; bgris; Verdier, O.; Karlsson, J.; zickert; Palenstijn, W. J.; ktem, O.; Chen, C.; Loarca, H. A.; Lohmann, M. odlgroup/odl: ODL 0.7.0. 2018; DOI: 10.5281/zenodo.1442734.
(45) van Aarle, W.; Palenstijn, W. J.; De Beenhouwer, J.; Altantzis, T.; Bals, S.; Batenburg, K. J.; Sijbers, J. The ASTRA Toolbox: A Platform for Advanced Algorithm Development in Electron Tomography. *Ultramicroscopy* **2015**, *157*, 35−47.

(46) Dengler, J. A Multi-Resolution Approach to the 3D Reconstruction from an Electron Microscope Tilt Series Solving the Alignment Problem without Gold Particles. *Ultramicroscopy* **1989**, *30*, 337−348.
(47) Ren, D.; Ophus, C.; Chen, M.; Waller, L. A Multiple Scattering Algorithm for Three Dimensional Phase Contrast Atomic Electron Tomography. *Ultramicroscopy* **2020**, *208*, 112860.
(48) Xu, R.; Chen, C.-C.; Wu, L.; Scott, M.; Theis, W.; Ophus, C.; Bartels, M.; Yang, Y.; Ramezani-Dakhel, H.; Sawaya, M. R.; Heinz, H.; Marks, L. D.; Ercius, P.; Miao, J. Three-Dimensional Coordinates of Individual Atoms in Materials Revealed by Electron Tomography. *Nat. Mater.* **2015**, *14*, 1099−1103.
(49) Yalisove, R.; Sung, S. H.; Ercius, P.; Hovden, R. Limits of Three-Dimensional Resolution and Dose for Aberration-Corrected Electron Tomography. *Phys. Rev. Appl.* **2021**, *15*, 014003.
(50) Hovden, R.; Ercius, P.; Jiang, Y.; Wang, D.; Yu, Y.; Abruña, H. D.; Elser, V.; Muller, D. A. Breaking the Crowther Limit: Combining Depth-Sectioning and Tilt Tomography for High-Resolution, Wide-Field 3D Reconstructions. *Ultramicroscopy* **2014**, *140*, 26−31.
(51) Lee, J.; Jeong, C.; Yang, Y. Single-Atom Level Determination Of 3-Dimensional Surface Atomic Structure via Neural Network-Assisted Atomic Electron Tomography. *Nat. Commun.* **2021**, *12*, 1962.
(52) Ullrich, K.; Berg, R. v. d.; Brubaker, M. A.; Fleet, D. J.; Welling, M. Differentiable Probabilistic Models of Scientific Imaging with the Fourier Slice Theorem. Proceedings of the Conference on Uncertainty in Artificial Intelligence (UAI). *arXiv*, 2019, https://arxiv.org/abs/1906.07582.
(53) McInnes, L.; Healy, J.; Melville, J. UMAP: Uniform Manifold Approximation and Projection for Dimension Reduction. *arXiv (Machine Learning)* 2020, http://arxiv.org/abs/1802.03426, (accessed Nov 1, 2021).
(54) Pedregosa, F.; Varoquaux, G.; Gramfort, A.; Michel, V.; Thirion, B.; Grisel, O.; Blondel, M.; Prettenhofer, P.; Weiss, R.; Dubourg, V.; Vanderplas, J.; Passos, A.; Cournapeau, D.; Brucher, M.; Perrot, M.; Duchesnay, E. Scikit-learn: Machine Learning in Python. *Journal of Machine Learning Research* **2011**, *12*, 2825−2830.
(55) Attias, H. *A Variational Bayesian Framework for Graphical Models*; Advances in Neural Information Processing Systems; MIT press: Boston, MA, 2000; Vol. *12*; pp 209−215.
(56) Ophus, C. A Fast Image Simulation Algorithm for Scanning Transmission Electron Microscopy. *Advanced Structural and Chemical Imaging* **2017**, *3*, 13.
(57) Rangel DaCosta, L. R.; Brown, H. G.; Pelz, P. M.; Rakowski, A.; Barber, N.; O'Donovan, P.; McBean, P.; Jones, L.; Ciston, J.; Scott, M.; Ophus, C. Prismatic 2.0 - Simulation Software for Scanning and High Resolution Transmission Electron Microscopy (STEM and HRTEM). *Micron* **2021**, *3*, 15.
(58) Besl, P.; McKay, N. D. A Method for Registration Of 3-D Shapes. *IEEE Transactions on Pattern Analysis and Machine Intelligence* **1992**, *14*, 239−256.
(59) Kjer, H. M., Wilm, J. Evaluation of Surface Registration Algorithms for PET Motion Correction. B.S. Thesis, Technical University of Denmark, Kongens Lyngby, Denmark, 2010.
(60) Steinhardt, P. J.; Nelson, D. R.; Ronchetti, M. Bond-Orientational Order in Liquids and Glasses. *Phys. Rev. B: Condens. Matter Mater. Phys.* **1983**, *28*, 784−805.

https://doi.org/10.1021/acsnano.1c07772
ACS Nano 2022, 16, 588−596